Materials & Design 238 (2024) 112708

Contents lists available at ScienceDirect

Materials & Design

journal homepage: www.elsevier.com/locate/matdes

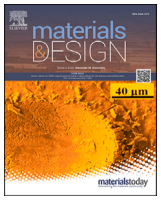

Phase-field modelling of failure in ceramics with multiscale porosity

R. Cavuoto [a], P. Lenarda [b], A. Tampieri [c], D. Bigoni [d,*], M. Paggi [b,*]

[a] School of Engineering, University of Naples "Federico II", Naples, Italy
[b] IMT School for Advanced Studies Lucca, Piazza San Francesco 19, 55100 Lucca, Italy
[c] Institute of Science and Technology for Ceramics, National Research Council, Via Granarolo 64, 48018 Faenza, Italy
[d] Instabilities Lab, University of Trento, Via Mesiano 77, Trento, 38123 Italy

ARTICLE INFO

Keywords:
Porous materials
Multiscale porosity
Bio-mimetic materials
Phase field approach to fracture
Finite element method

ABSTRACT

Many stiff biological materials exhibiting outstanding compressive strength/weight ratio are characterized by high porosity, spanning different size-scales, typical examples being bone and wood. A successful bio-mimicking of these materials is provided by a recently obtained apatite, directly produced through a biomorphic transformation of natural wood and thus inheriting its highly hierarchical structure. This unique apatite (but also wood and bone) is characterized by two major distinct populations of differently-sized cylindrical voids, a porosity shown in the present paper to influence failure, both in terms of damage growth and fracture nucleation and propagation. This statement follows from failure analysis, developed through in-silico generation of artificial samples (reproducing the two-scale porosity of the material) and subsequent finite element modelling of damage, implemented with phase-field treatment for fracture growth. It is found that small voids promote damage nucleation and enhance bridging of macro-pores by micro-crack formation, while macro-pores influence the overall material response and drive the propagation of large fractures. Our results explain the important role of multiscale porosity characterizing stiff biological materials and lead to a new design paradigm, by introducing an in-silico tool to implement bio-mimicking in new artificial materials with brittle behaviour, such as carbide or ceramic foams.

1. Introduction

Materials characterized by a high-density distribution of voids are diffused in nature (for instance bone, wood, rock –sandstone, tuff, pumice–, coal) and as man-made materials (for instance concrete, cellular ceramic, and carbide foam). Wood and bone evidence populations of cylindrical pores with nearly circular cross-sections, ranging in diameter through multiple size scales, a feature affecting many of their physical [1–3] and mechanical [4–6] properties. Implementing size-scale variation in the porosity of artificial materials is a bio-mimicking challenge, particularly for bone substitutes and scaffolds [7–11]. A successful answer to this challenge was provided [12] through the synthesis of a new material, a 3-D porous apatite (called 'Biomorphic Apatite', BA in the following) obtained via a bio-morphic transformation of natural wood into ceramics, Fig. 1.

BA replicates the multiscale hierarchical structure of wood, with a double-sized porosity (Fig. 1), sharing similarities with bone and thus becoming ideal for bio-mechanical applications, where outstanding strength and fracture energy absorption are crucially important [1,13]. Here, a correct failure analysis may lead to the design of surgical interventions and prediction of rehabilitation times so that the development of a numerical tool for this analysis is the object of the present paper. A class of materials (including those addressed here, plus glass, ceramic, rock and concrete) are brittle so that fracture nucleates primarily under tensile stresses. Under overall compression, crack generation is complicated by the presence of voids, which concentrate tensile stress near their boundary and stimulate fracture growth parallel to the loading direction [14–16], see Fig. 1. Fracture patterns are typically tortuous and difficult to follow or model analytically [17], so that numerical techniques play a decisive role. These can be classified as: (i.) augmented versions of the finite-element method [18] (such as cohesive-zone methods, CZM, or extended finite-element methods, XFEM, the former requiring an initial knowledge of the crack pattern and the latter an *ad hoc* constitutive relation at the crack tip); (ii.) diffusive damage models [19–22] (relying on a regularized crack topology); (iii.) the phase-field approach, overcoming the difficulties encountered in the other techniques by allowing damage to grow within a thin portion of the material. The latter technique has been developed as

* Corresponding authors.
E-mail addresses: bigoni@ing.unitn.it (D. Bigoni), marco.paggi@imtlucca.it (M. Paggi).

https://doi.org/10.1016/j.matdes.2024.112708
Received 5 April 2023; Received in revised form 25 January 2024; Accepted 26 January 2024
Available online 1 February 2024

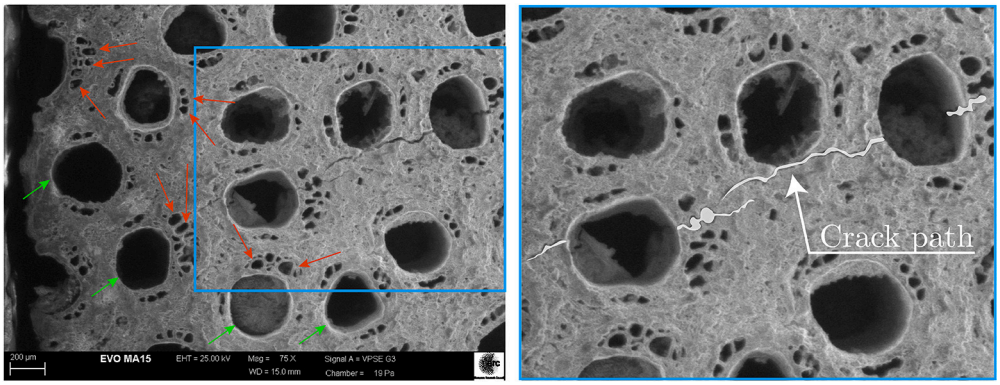

Fig. 1. Crack propagation in Biomorphic Apatite, characterized by a multiscale porosity. Left: SEM image of a BA sample characterized by the presence of macro (green arrows) and meso (red arrows) cylindrical pores with a nearly circular cross-section. The sample was subjected to uniaxial compression test. Right: a magnified detail of the sample on the left shows a crack (highlighted white) which nucleated, almost parallel to the direction of loading, from the external surface of a macro pore, where tensile stress locally develops, although the mean stress in the sample is compressive.

an energy minimization, via Γ-convergence regularization of free discontinuities to model cracks [23–30] and was recently proven to be particularly suitable for the description of complex fracture patterns in PMMA samples with notches and holes [31] and therefore is adopted here.

The porosity typical of biomorphic apatite is primarily double-sized so that macro-scale pores can be differentiated from meso-scale pores, Fig. 1 (micropores, also present, are neglected as they were found not to influence fracture) and is shown to correspond to two peaks of a probability density function. This function allows the set-up of a numerical tool for the generation of in-silico porous samples, to be used for subsequent fracture simulation using the phase-field technique.

The simulations show that the porosity is always connected to a reduction of the overall stiffness and strength of the material. However, the meso-scale porosity produces: (i.) a smearing of damage through zones that would remain intact in the absence of this scale of pores; (ii.) a shielding of regions of the material from cracks; and (iii.) a promotion of fracture growth in other zones.

Our results show that, not only the value of 'total porosity' is relevant to the mechanical modelling of porous-brittle solids, but also the amount of fractions of porosity with different characteristic size plays a decisive role, a result with implications in the simulation of fracture in biological porous materials, such as bone or wood, and in porous ceramics for bone repair or for filters used in industrial applications.

2. Results

2.1. Theory

In a purely isothermal formulation of a brittle-damaging material, where the damage only occurs for tensile strains, the Helmholtz free energy per unit volume can be represented as

$$\psi(\boldsymbol{\varepsilon}, s) = \left[(1-s)^2 + k\right] \psi_+(\boldsymbol{\varepsilon}) + \psi_-(\boldsymbol{\varepsilon}), \tag{1}$$

a function of a damage parameter $s \in [1-\sqrt{1-k}, 1]$, where $k > 0$ represents a residual stiffness and $\boldsymbol{\varepsilon}$ is the strain. Note that the lower bound of the range of variation for s corresponds to an intact material, while $s = 1$ to a fully damaged one. Equation (1) embodies an additive split of the elastic energy $\psi(\boldsymbol{\varepsilon})$ into tensile, '+', and compressive, '−', strains

$$\boldsymbol{\varepsilon}_\pm = \sum_{i=1}^{3} \langle \varepsilon_i \rangle_\pm \boldsymbol{e}_i \otimes \boldsymbol{e}_i, \tag{2}$$

where $\boldsymbol{e}_i$ and ε_i $(i = 1, 2, 3)$ are the unit eigenvectors and corresponding eigenvalues of the strain, respectively, and $\langle \cdot \rangle$ denotes the Macaulay bracket operator, defined for every scalar x as $\langle x \rangle_\pm = (x \pm |x|)/2$. Following [29] the tensile and compressive parts of the strain energy density assume the following expression:

$$\psi_\pm(\boldsymbol{\varepsilon}) = \frac{\lambda}{2} \langle \pm \mathrm{tr}\boldsymbol{\varepsilon} \rangle^2 + \mu \mathrm{tr}\left(\boldsymbol{\varepsilon}_\pm^2\right), \tag{3}$$

where λ and μ are the Lamé constants and $\mathrm{tr}(\cdot)$ denotes the trace operator.

The Helmholtz free energy, Eq. (1), defines a diffuse and isotropic damage model, where damage only occurs in tension, so that the stress tensor

$$\boldsymbol{\sigma}(\boldsymbol{\varepsilon}, s) = \frac{\partial \psi(\boldsymbol{\varepsilon}, s)}{\partial \boldsymbol{\varepsilon}} \tag{4}$$

becomes the work-conjugate to the strain and is represented as the sum between tensile and compressive components, $\boldsymbol{\sigma} = \boldsymbol{\sigma}_+ + \boldsymbol{\sigma}_-$, both related to the strains through the isotropic elasticity tensor $\mathbb{C}$ as

$$\boldsymbol{\sigma}_+ = \left[(1-s)^2 + k\right] \mathbb{C}\boldsymbol{\varepsilon}_+, \qquad \boldsymbol{\sigma}_- = \mathbb{C}\boldsymbol{\varepsilon}_-. \tag{5}$$

Following the variational approach to brittle fracture, propagation and branching of a crack in a damaging solid can be found as the result of the minimization of the energy functional [29,32]

$$\Pi(\mathbf{u}, s, \Gamma) = \int_{\Omega \setminus \Gamma} \psi(\boldsymbol{\varepsilon}, s)\, \mathrm{d}\mathbf{x} + \int_{\Gamma} \mathcal{G}_c(s)\, \mathrm{d}\Gamma, \tag{6}$$

where $\mathbf{u}$ is the displacement, $\mathcal{G}_c$ is the fracture energy and Γ is the (unknown and evolving) fracture path inside the body Ω.

A direct use of the functional (6) involves the solution of a free boundary value problem, which can be approximated by following the regularized framework introduced with the phase field approach [24,29]. The approximation regards the topology of the crack, which is smeared out onto the whole body, allowing to rewrite the potential energy of the system as a volume integral

$$\Pi(\mathbf{u}, s) = \int_{\Omega} \left[\psi(\boldsymbol{\varepsilon}, s) + G_c\, \gamma(s, \nabla s)\right] \mathrm{d}\mathbf{x}\,, \tag{7}$$

where $\gamma(s, \nabla s)$ is the crack density functional, depending on the spatial gradient $\nabla\cdot$ of the internal state variable s, now called 'phase field variable'.

The surface Γ, not explicitly present in the functional (7), can be recovered as the result of an energy minimization procedure. In particular, introducing the so-called 'AT2 model' [26,29], the functional $\gamma(s, \nabla s)$ is represented by the following convex function

$$\gamma(s, \nabla s) = \frac{1}{2l} s^2 + \frac{l}{2} |\nabla s|^2\,, \tag{8}$$

where l is a regularization characteristic length, related to the smeared crack width. For a sufficiently small l, the minimization of functional

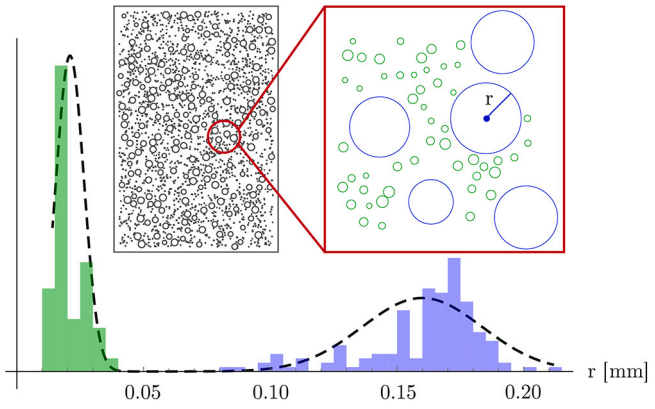

Fig. 2. Size distribution of voids in Biomorphic Apatite, characterized by multiscale porosity. Probability density function (PDF, shown dashed) obtained from SEM photomicrographs of BA samples, modelling their void distribution in terms of the voids' radius, r. The BA specimens evidence a bimodal distribution of void radii typical of a double porosity (macro-porosity is marked in blue, while meso-porosity in green). The inset shows a sample generated in-silico with the PDF reported in Fig. (black dashed curve), which has been coupled with a random generator to impose the position of the voids' centre.

(7), implemented with the nonlocal crack density function (8), 'spontaneously' leads to a solution where the damage is strongly localized near a surface Γ, representing a crack. Formally, it can be demonstrated that, for vanishing regularization parameter ($l \to 0$), the formulation outlined in Eq. (7) tends to Eq. (6) in the sense of the so-called 'Γ-convergence' [28].

Finally, the weak form of the variational problem, and the consequent finite-element discretization, can be found in [31].

3. Virtual testing

3.1. Two scale porosity and mesh generation

A brittle porous material is now considered, characterized by a two-scale cylindrical porosity. A two-dimensional formulation fits the specific *transverse* structure that biomorphic apatite ('BA' henceforth) inherits from rattan wood, which presents elongated grains and parallel channels, with approximately circular cross-section and two predominant sizes (Fig. 1).

The BA samples are characterized by three size-levels of porosity $0 \leq \Phi \leq 1$ (defined as the ratio between the volume of voids and the total volume of the element in a representative volume element), namely, macroscopic (approximately 300 μm in diameter), mesoscopic (up to 50 μm in diameter), and microscopic (1 μm of diameter) [1]. Thus, while the size ratio between mesoporosity and macroporosity ranges within the interval (1/15, 1/2), the size ratio between microporosity and macroporosity is smaller than 1/100. Therefore, the microporosity has then been assumed to be part of the matrix. Using an *ad hoc* developed Matlab code (based on image analysis functions 'imread' and 'imfindcircles', available in the complementary material), the porosity of BA, as characterized from SEM photomicrographs, was shown to obey to the following probability distribution function (PDF)

$$f = 16.82\, \mathrm{e}^{-889.1(r-0.16)^2} + 72.24\, \mathrm{e}^{-16396(r-0.02)^2}, \tag{9}$$

which exhibits a bi-modal shape, clearly visible in Fig. 2 (black dashed curve).

The peak on the right of the curve occurs at high values of void radius and is representative of macro-porosity Φ_{macro}, while the peak on the left is representative of meso-porosity Φ_{meso}, so that, neglecting the micro level, the total porosity is the sum of the two following major contributions $\Phi = \Phi_{\mathrm{macro}} + \Phi_{\mathrm{meso}}$.

The obtained PDF was used for in-silico generation (through random placement of non-overlapping voids) of samples of porous materials (an example is shown in the inset of Fig. 2), needed for simulations (performed at the Laboratory for Numerical Modelling of Materials of the University of Trento, using a Workstation AMD Ryzen Threadripper PRO 5995WX, 512 GB RAM, 2 GeForce RTX 3090 graphic cards, acquired with the ERC-AdG-2021-101052956-Beyond), via the previously outlined phase-field approach.

In order to investigate the influence of two size-scale porosity on crack patterns in ceramic materials subject to uniaxial compression, a preliminary calibration (reported in the supporting material) on single-porosity samples [generated by simply neglecting the right term in equation (9)] has been performed for both mechanical model and mesh size for subsequent finite element solution. The results of this analysis are shown in the supporting material.

For a material characterized by a porosity Φ, independently of the number of size-scales of porosity, the overall stiffness of an equivalent homogeneous material can theoretically be estimated in a number of ways. For spherical voids, results applicable to ceramic materials were provided in [33–35]. For cylindrical voids, the generalized self-consistent homogenization scheme [36] is followed. The effective Young's modulus $\bar{E}$, defining a homogeneous elastic solid under plane stress, is given by

$$\frac{\bar{E}}{E_{\mathrm{matrix}}} = \frac{\Phi(1-2\Phi-\Phi^2) + \sqrt{(1+\Phi+\Phi^2+\Phi^3)^2 - 12\Phi^2}}{1+5\Phi+2\Phi^2}, \tag{10}$$

which will be used in the following as a reference.

The peak stress under increasing uniaxial stress $\bar{\sigma}$ (corresponding to failure in a force-controlled testing device), for a sample made of an equivalent homogeneous material, is assumed to follow the simple rule [37]

$$\frac{\bar{\sigma}}{\sigma_{\mathrm{matrix}}} = \mathrm{e}^{-b\Phi}, \tag{11}$$

where σ_{matrix} is the peak (or failure) stress in the matrix material and b a coefficient to be fitted with measurements, which in our case was found to be $b \approx 6.17$.

Equations (10) and (11) are used as a reference in the simulations, in particular, once Young's modulus and failure stress of the matrix material are assigned for numerical calculations, the above equations are employed to obtain an expected 'rough' behaviour of porous samples. Simulations of uniaxial compression tests have been performed for values of (single-scale) macro-porosity equal to {5%, 10%, 15%, 20%, 25%, 30%, 35%, 40%} (see Fig. 3, upper part), and the material parameters used throughout the numerical simulations are: E = 70 MPa, $\nu = 0,25$, $\mathrm{G_c} = 0.0025$ MPa mm, l = 0.12 mm. For each value of porosity, ten specimens with different distributions of pores have been considered and, accordingly, ten different overall stress/strain responses have been obtained [in terms of $\bar{\sigma}$ = (measured force)/(cross-section area) and $\bar{\varepsilon}$ = (applied displacement)/L]. For each value of macro-porosity $(5\%, 10\%, 15\%, 20\%, 25\%, 30\%, 35\%, 40\%)$ the mean response evaluated over ten simulated stress-strain curves is reported in Fig. 3. Further results for three (of the ten) samples characterized by a macro porosity of 20% are shown in Fig. 4.

Here, in full agreement with experimental results, simulations show that the response of the specimens remains almost linear until a peak value of stress is reached, and it is followed by a softening branch, due to the coalescence of small cracks.

It should be noted that the overall stress/strain curves shown in Fig. 4 are plotted up to values of overall strain equal to 0.11. Although moderately high, these strains can be decomposed into small strains in the matrix material and rigid-body displacements related to failure. Therefore, local strains remain moderate, as further detailed in the Supporting material.

The shape of the softening branch and the value of the peak stress greatly depend on the geometrical distribution of voids, while the stiff-

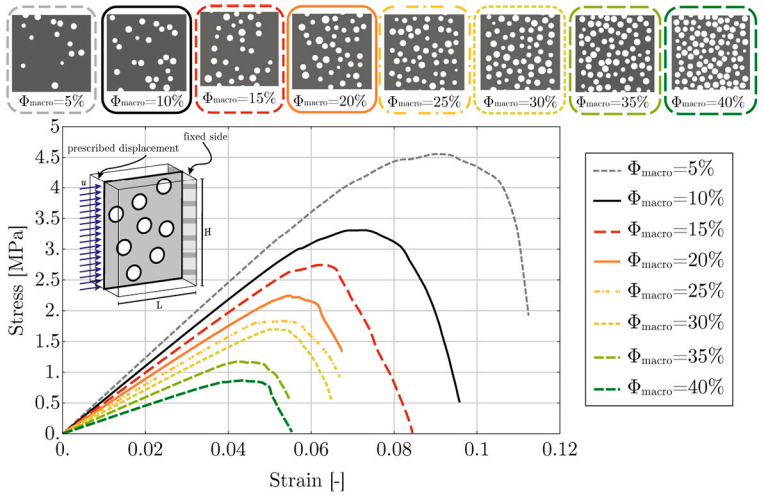

Fig. 3. Response to compression of biomorphic apatite, where only one scale of porosity is considered. Mean value (over 10 different porosity distributions) of the stress-strain response for single-porosity samples, for different values of macro-porosity, Φ_{macro}. A qualitative example of the analyzed in-silico generated sample with the prescribed boundary conditions is shown in the left inset of the stress-stress plot.

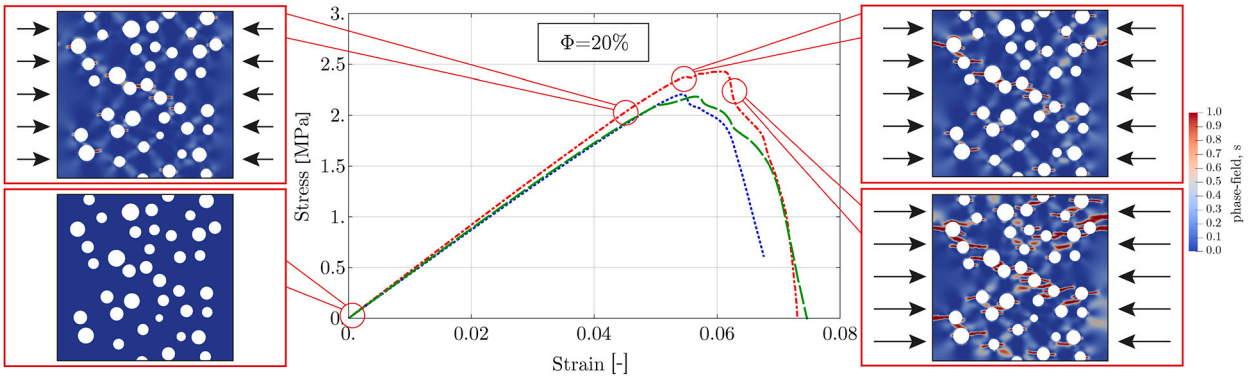

Fig. 4. Compression behaviour of a simulated biomorphic apatite, where only one scale of porosity is considered, using phase-field. Simulated overall stress-strain responses for three samples with the same porosity 20%, but different void distributions. The progressive crack formation and growth, developing parallel to the load direction, is reported at increasing values of overall strain $\bar{\varepsilon}$ in the inset for the sample with $\Phi_{macro} = 20\%$ shown unloaded in Fig. 3 of the supporting material. Note the strong effect of crack propagation on the overall stress-strain curves.

ness (the tangent line to the stress-strain curve) is only slightly influenced. Fig. 4 is enhanced with insets, showing crack growth at different test stages, developing parallel to the direction of applied loading. The last feature, agreeing with experiments, reveals that the model can effectively capture damage nucleation, fracture propagation and the final failure mechanism.

The mean value and standard deviation of overall stiffness (Young's modulus $\bar{E}$) and strength (peak stress $\bar{\sigma}$) are reported in Table 1, evaluated using simulations pertaining to the ten specimens tested for each porosity level. Predictions obtained with Eqs. (10) and (11) are included in parentheses and show a tight agreement with the numerical values. It can be noted from the table that at an increase of macro-porosity, the effect of the void distribution on the overall strength tends to decrease, while the stiffness remains almost constant.

Fig. 5 summarizes results for specimens characterized by a single-scale porosity, by displaying values of peak stress and stiffness, as functions of the amount of porosity. Data agree well with predictions from micromechanical models, Eqs. (10) and (11).

3.2. Compression test on porous brittle solids: two-scale porosity

The phase-field approach to fracture mechanics is shown now to answer several questions that may arise when modelling or designing

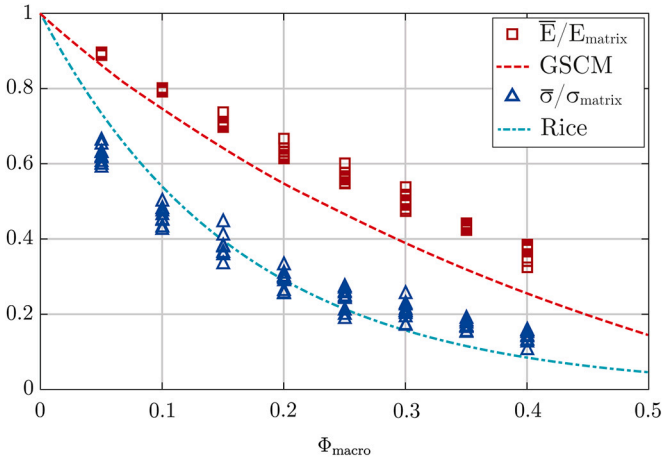

Fig. 5. Overall response of in-silico generated samples of Biomorphic Apatite, where only one scale of porosity is considered. Simulated overall peak stress $\bar{\sigma}$ (triangular spots) and overall Young's Modulus $\bar{E}$ (square spots) as functions of macro-porosity, Φ_{macro}. Theoretical predictions from micromechanical models, Eqs. (10) and (11), respectively denoted with 'GSCM' and 'Rice', are also reported.

Table 1
Overall properties of compressed Biomorphic Apatite samples (generated in silico), where only one scale of porosity is considered. Mean value (denoted as 'Mean') and standard deviation (denoted as 'St. Dev') of overall Young's Modulus $\bar{E}$ and peak stress $\bar{\sigma}$ for different values of macro-porosity, as obtained from simulations of compression tests. Quantities are expressed in MPa. Values obtained with the self-consistent method and that proposed by Rice, respectively Eqs. (10) and (11), are reported in parentheses.

	$\Phi_{macro} = 5\%$	10%	15%	20%	25%	30%	35%	40%
Mean($\bar{E}$)	61.9 (60.4)	55.2 (52.3)	49.1 (45.1)	43.5 (38.7)	38.9 (32.9)	34.4 (27.6)	29.8 (22.7)	25.2 (18.2)
Mean($\bar{\sigma}$)	4.53 (5.38)	3.34 (3.99)	2.76 (2.96)	2.13 (2.19)	1.76 (1.62)	1.53 (1.20)	1.25 (0.89)	1.04 (0.66)
St. Dev($\bar{E}$)	0.17	0.22	0.79	1.06	1.15	1.29	0.46	1.57
St. Dev($\bar{\sigma}$)	0.17	0.17	0.23	0.18	0.21	0.18	0.08	0.12

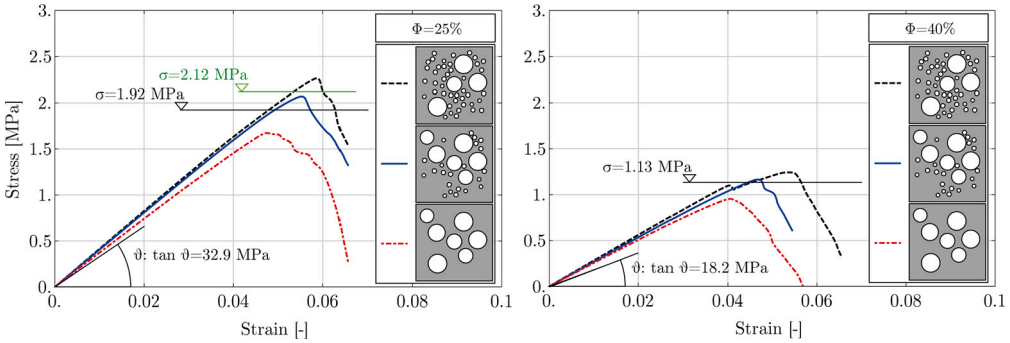

Fig. 6. Influence of multiscale porosity on the overall behaviour of Biomorphic Apatite samples (generated in silico). The effects related to the presence of meso-pores are visible in the simulated overall stress-strain responses for samples characterized by the same value of total porosity Φ (25% on the left and 40% on the right), but different amounts of meso Φ_{meso} and macro Φ_{macro} porosity. The Young's modulus $\bar{E} = \tan\theta$ and peak stress $\bar{\sigma}_{peak}$, Eqs. (10) and (11), are included. Peak stress and elastic stiffness increase when the density of meso-pores is increased. The value $\sigma = 2.12$ MPa reported in green is the mean value of peak stress measured on 4 compression tests on biomorphic apatite, very well captured by the simulations.

functional porous ceramics. In particular, at a fixed value of total porosity (7 values are explored, see Appendix A.6), simulations on in-silico created samples are used with different percentages of macro and meso voids, to explore effects related to second-scale porosity on: (i.) overall Young's modulus, (ii.) failure stress, (iii.) crack growth, and (iv.) damage diffusion.

Overall stress/strain curves, analogous to those presented in Fig. 4, but now computed for double-scale porosity, are depicted in Fig. 6. Here, the total porosity (sum of the macro and meso values, $\Phi = \Phi_{macro} + \Phi_{meso}$) is assumed to be equal to 25% (left) and 40% (right). Each curve represents the response of a sample in which the overall porosity is achieved by mixing different portions of macro-pores and meso-pores, where the former pores have a larger size than the latter, according to the PDF, Eq. (9). The peaks of the curves shown in Fig. 6 reveal that a superior mechanical response for specimens follows from an increase in the percentage of meso-pores. The left image of the same figure shows a specimen with total porosity of 25% split in macro-porosity and meso-porosity as follows: the red dot-dashed curve is characterized by 25% of macro-porosity, the blue one by 20% macro-porosity and 5% meso-porosity, and lastly, the black dashed one by 15% macro-porosity and 10% meso-porosity. The image on the right shows the effect is reproduced also for a total porosity of 40%. Note that the figure also reports (in green) the mean value of peak stress, 2.12 MPa, obtained from 4 experiments on biomorphic apatite, as reported in Table 2, which agrees very well with the simulations. The table reports also the value of peak stress as obtained from the simulation with the void distribution tighter to the real specimens.

Overall properties, in terms of peak strength and elastic modulus, for different specimens are shown in Fig. 7, as functions of the total porosity, but for different values of meso (and thus also macro) porosity. According to [38], the figure reveals that for a fixed value of total porosity, samples display improved mechanical properties at low macro porosity (triangles are located clearly above the trend lines). Therefore, macro porosity is more detrimental to stiffness and strength than

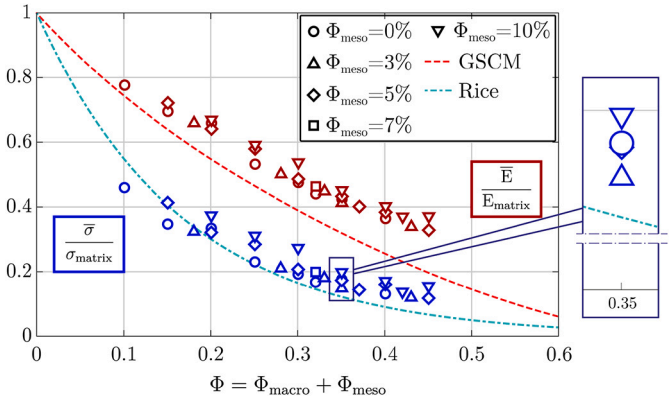

Fig. 7. Overall properties of Biomorphic Apatite samples (generated in silico), with pores of different sizes. Simulated dimensionless Young's modulus (red symbols) and peak stress (blue symbols) versus total porosity for samples characterized by double porosity. The inset shows that at $\Phi = 0.35$, the presence of a 0.03 fraction of meso-porosity can (surprisingly and contrary to most of the results) lead to a smaller stiffness and strength than the case where meso-porosity is absent. This is related to the specific geometrical distribution of voids. Theoretical predictions from micromechanical models, Eqs. (10) and (11), respectively denoted with 'GSCM' and 'Rice', are also reported.

meso-porosity. However, our computations show that this is not a strict rule, as evidenced in the inset of Fig. 7, showing that a sample at 0.35 total-porosity with 0.03 meso-porosity is less stiff and resistant than the sample with null meso-porosity. This feature is not isolated and occurs also at $\Phi = 0.2$ and is related to the particular geometrical distribution of voids and prompts the idea that the design of the spatial void distribution (possible via phase field) could improve material performances.

Both scales of porosity are found to concur in producing a non-linear effect on the overall properties of the porous material. In particular, an

Table 2
Comparison between the peak stress resulting from a numerical simulation (using the phase-field technique on a sample with a porosity distribution representative of the real specimens) and from a compression test on four samples of a Biomorphic Apatite with 27% porosity (Samples 1–4).

	Numerical	Sample 1	Sample 2	Sample 3	Sample 4	Mean
Peak Stress [MPa]	2.06	2.33	2.17	2.03	1.93	2.12

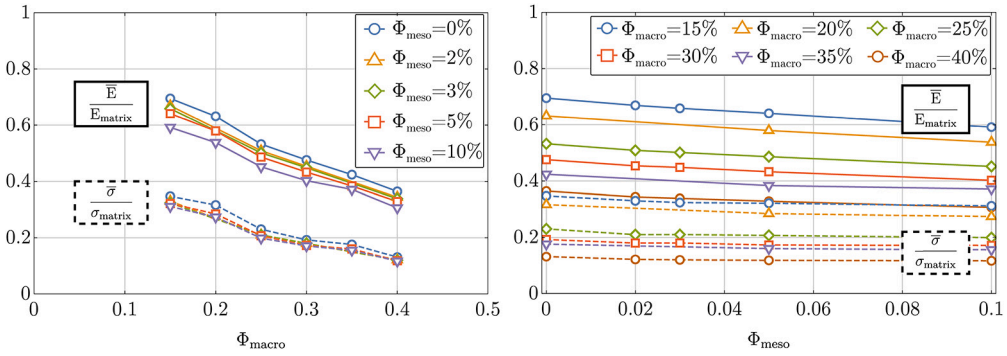

Fig. 8. Dependence of the mechanical behaviour of Biomorphic Apatite on the voids' size distribution. Effects of the meso porosity fraction on the dimensionless peak stress and Young's modulus as a function of the macro porosity (left) and vice-versa (right).

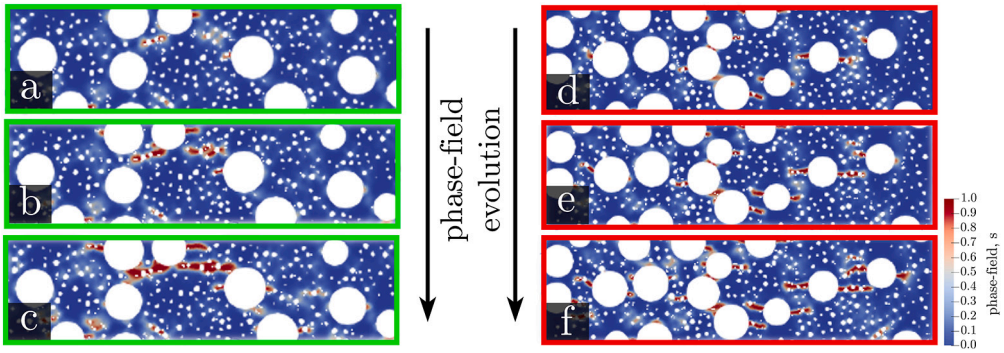

Fig. 9. Crack evolution in Biomorphic Apatite with multiple scale porosity using the phase-field. Simulated fracture evolution through phase-field during compression of a sample characterized by a macro-porosity $\Phi_{macro} = 25\%$ and meso-porosity $\Phi_{meso} = 10\%$. Meso-pores induce two failure mechanisms, either involving nucleation (a-b) and growth (c) of cracks, or connecting macro-pores (d-e) and ultimately leading to failure (e).

interaction is observed between the two scales of porosity (the sum between the two Φ_{macro} and Φ_{meso} is constant and equal to Φ). This emerges from the plots of the dimensionless peak strength and Young's modulus reported in Fig. 8 as resulting from simulated stress-strain curves, functions of macro and meso-porosity Φ_{macro} and Φ_{meso}. Simple linear regression of the normalized overall properties obtained from our two-scale porosity analyses (depicted in Fig. 8) leads to the following approximations

$$\frac{\overline{E}}{E_{matrix}} = 0.905 - 1.401\Phi_{macro} - 0.868\Phi_{meso},\ R^2 = 0.913, \tag{12}$$

$$\frac{\overline{\sigma}}{\sigma_{matrix}} = 0.610 - 1.303\Phi_{macro} - 0.704\Phi_{meso},\ R^2 = 0.748, \tag{13}$$

where R^2 is the coefficient of determination.

Crack patterns are found to be strongly influenced by meso-porosity at fixed values of macro-porosity, as shown in Fig. 9, where simulations of crack patterns in two portions of a sample (one framed green and the other red) are shown at different stages of loading, during a compression test for $\Phi_{macro} = 25\%$ and $\Phi_{meso} = 10\%$. Here, simulations reveal the existence of two mechanisms of failure affecting specimens characterized by double porosity: (i.) in the portion of the sample framed red, cracks nucleate at the edge of macro-pores, while meso-pores promote the development of a crack network, while (ii.) in the portion framed green, cracks nucleate near meso-pores and develop by joining macro-pores.

Crack paths in two-scale porous specimens. The presence of meso-porosity does not only affect the overall mechanical behaviour of a specimen in terms of stiffness and strength, but also its failure. The meso-porosity enhances damage diffusion and promotes new fracture paths, different from those observed in the absence of meso pores, as visible in Fig. 10, for $\Phi_{macro} = 20\%$. Here crack patterns are analyzed in a region of a sample compressed at a fixed value $\bar{\varepsilon} = -6.1 \times 10^{-2}$ of overall strain, but with different amounts of meso-porosity, equal to {0%, 5%, 10%}. In the region reported on the left, the meso porosity diffuses the damage and inhibits macro crack growth. Differently, on the right, meso porosity, initially enhances crack growth through bridging of microcracks (compare results at $\Phi_{meso} = 0$ and 10%), while a further increase in meso porosity shields the material from macrocracking.

Direct comparisons between phase-field simulations of fracture growth in a porous material and micrographs obtained during compression tests on BA (performed at the MUSAM-Lab, financed with the ERC StG CA2PVM, Grant Agreement 306622, and the ERC PoC PHYSIC, Grant Agreement No. 737447, at IMT School, Lucca), is presented in Fig. 11. The tests were executed by placing prismatic samples in direct contact with two steel platens (lateral size 40 mm and thickness

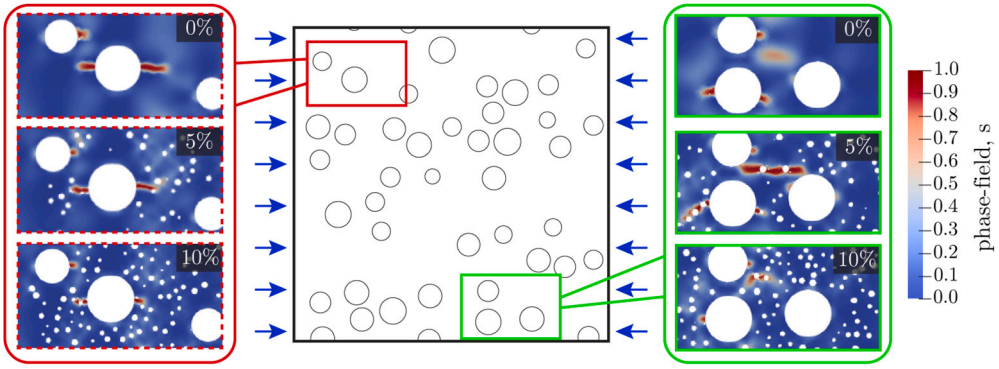

Fig. 10. Effects of voids of small size on crack nucleation and growth in Biomorphic Apatite. Cracks develop parallel to the loading direction in the simulated fracture evolution through phase field during compression of a sample characterized by a macro porosity 20% and different values of meso-porosity equal to {0% 5%, 10%}. The reported phase-field refers to an overall strain of $\bar{\varepsilon} = -6.1 \times 10^{-2}$. Note that the amount of meso-porosity influences the mechanisms of fracture, so that an increase of this porosity may promote or inhibit crack growth.

5 mm) and compressed (using the tensile/compressive stage DEBEN 5000S inside the scanning electron microscope Zeiss EVO MA15) by imposing displacements. The tests were continued until complete failure of the samples. Two mechanisms of crack propagation can be observed in Fig. 11: cracks either nucleate in the proximity of large pores and develop horizontally (highlighted in the figure with green arrows), or they nucleate near meso pores, thus producing a fracture network, where macro and meso pores are connected (highlighted in the figure with white arrows). Results of simulations are not *coincident* with the fracture experiments, because the samples used for simulation are randomly generated and therefore not identical to those analyzed experimentally. Nevertheless, the mechanisms of crack nucleation and growth are the same.

Note that, while the test at higher magnification (reported in Fig. 11) was performed inside the SEM, the other was conducted in air with the same tensile/compressive stage, but examined with a confocal microscope (Leica DCM3D) with a magnification lens 10×. In this way, a larger portion of the sample was observed. Again, sub-horizontal cracks are observed (green arrows), connecting macro pores, while inclined cracks nucleated near meso pores and later coalesced to join a 'main' propagating crack (characterized by a characteristic tortuosity). Cracks originating from meso-pores can sometimes shield macro-pores, as clearly indicated by the white arrows. All these features are accurately reproduced in the simulations.

Fig. 12 presents a view of a failed sample at a larger scale than that of Fig. 11, right (photo taken in air with a confocal microscope Leica DCM3D). Here the simulation (reported in terms of phase field on the left and deformed mesh on the central part) captures the formation of an inclined zone of highly damaged material, where micro and macro cracks form a large, but localized, failure zone. Again, while the simulation was performed on a randomly generated specimen, the failure mode is strongly representative of real tests.

4. Discussion

Simulations carried out with the phase-field approach to fracture on samples with cylindrical porosity (generated in-silico to model a porous ceramics obtained from wood, biomorphic apatite) show that the presence of two size-scales of porosity plays an important role in damage diffusion and fracture growth. In particular, the simulations (performed with an in-house developed finite element code, calibrated on brittle materials, available in the Supplementary materials) show that during compressive failure: (i.) fractures nucleate at pore boundaries and grow almost parallel to the direction of compression; (ii.) large pores induce crack nucleation, while small pores foster their propagation by connecting distantly located voids; (iii.) small pores cause the formation of micro-cracks, eventually promoting and propagating fail-

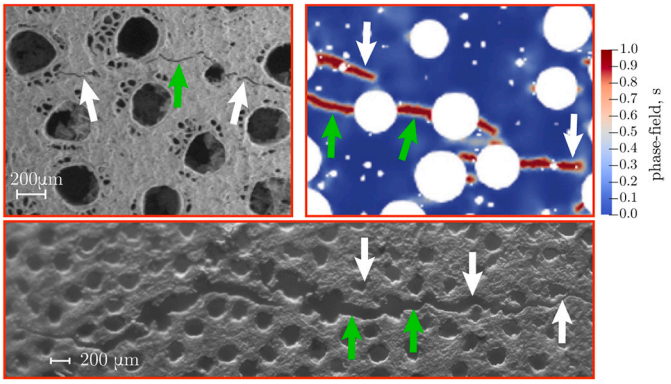

Fig. 11. Phase-field successfully reproduces crack propagation mechanisms in biomorphic apatite. Upper part on the left and lower part: experiments show crack propagation nearly parallel to the applied compressive stress. The same feature is found in the simulation on a randomly generated sample (thus not identical neither to the sample on the left nor to that in the lower part). The simulation was terminated at an overall strain of 6.5×10^{-2}. The photo in the upper part was made with a SEM, while the other with a confocal microscope (Leica DCM3D), during a compression test. Note that the tortuosity of the crack paths is the result of almost straight cracks connecting macro-pores (green arrows), while inclined cracks originate from micro-pores (white arrows).

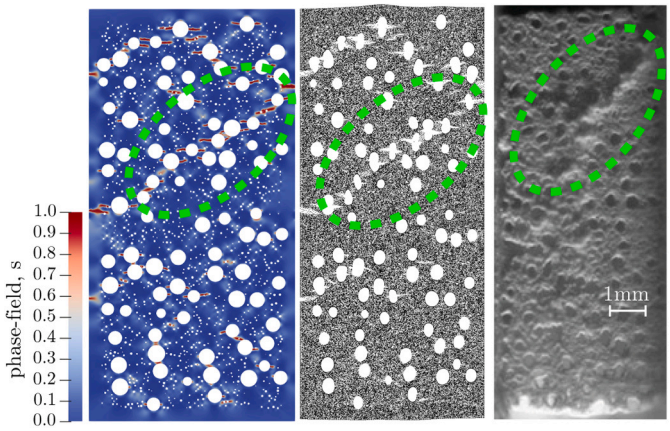

Fig. 12. The phase-field (left) and the deformed mesh (centre) successfully reproduces failure patterns in a biomorphic apatite with 27% total porosity (photo on the right). The simulation is performed on a sample with the same meso and macro porosity of the real material, but with a random generation of voids. Even if the real sample is not identical to that tested in silico, the failure mode is the same.

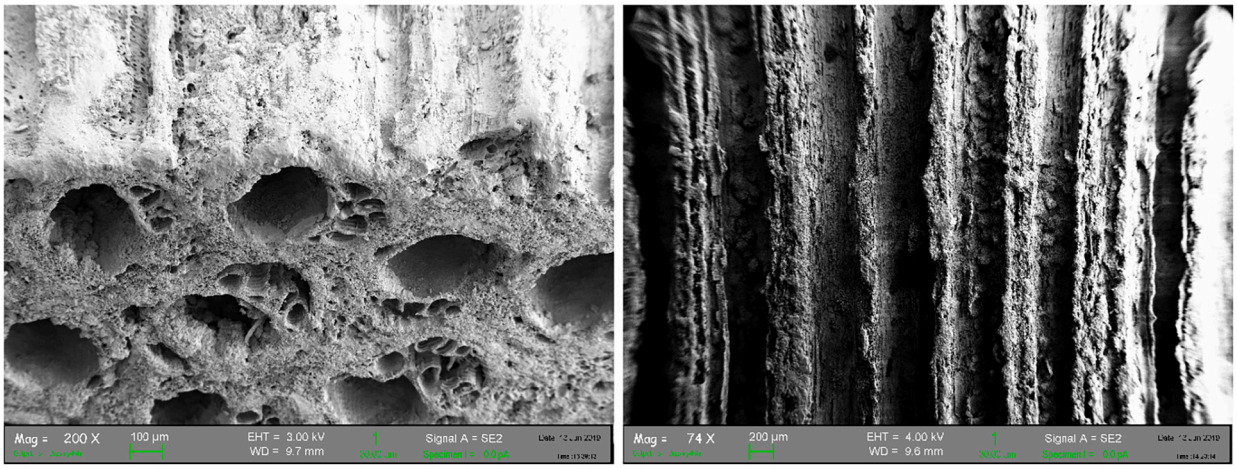

Extended Data Fig. 1. The microscopic structure of biomorphic apatite. Two SEM micrographs showing the cylindrical nature of the porosity of Biomorphic Apatite, resulting from the micromorphic transformation of rattan wood. The photo on the left shows two orthogonal planes, one crossing and the other parallel to the axes of the cylindrical voids. The photo on right pertains to a section of a sample taken parallel to the axes of the cylindrical voids.

ure; (iv.) small pores diffuse damage and reduce the inclination of the softening branches in the overall stress-strain curves.

At a given value of the total porosity, specimens characterized by high values of meso-porosity exhibit mechanical properties, expressed through Young's modulus and peak stress, which are superior to those displayed by specimens with the same porosity but uniform. Therefore, the pore size distribution has to be considered a major influential parameter in the mechanical design of porous brittle materials, where the phase-field approach reveals its excellent potentialities.

CRediT authorship contribution statement

R. Cavuoto: Conceptualization, Data curation, Formal analysis, Investigation, Methodology, Writing – original draft, Validation. **P. Lenarda:** Conceptualization, Data curation, Formal analysis, Investigation, Methodology, Validation, Writing – original draft, Writing – review & editing. **A. Tampieri:** Data curation, Resources, Visualization, Writing – original draft, Writing – review & editing. **D. Bigoni:** Conceptualization, Funding acquisition, Project administration, Supervision, Visualization, Writing – original draft, Writing – review & editing. **M. Paggi:** Conceptualization, Funding acquisition, Methodology, Supervision, Visualization, Writing – original draft, Writing – review & editing.

Declaration of competing interest

The authors declare that they have no known competing financial interests or personal relationships that could have appeared to influence the work reported in this paper.

Data availability

All the raw/processed data required to reproduce these findings are provided in the Appendix A, both in terms of finite element codes to generate and run the computational models, and in terms of key research results.

Acknowledgements

The authors acknowledge fruitful discussions with Professor Willi Pabst (Department of Glass and Ceramics, University of Chemistry and Technology, Prague, Czech Republic).

D.B. and R.C. acknowledge financial support from the European Research Council Advanced Grant scheme (ERC-AdG), under the European Union's Horizon 2020 research and innovation programme (Grant agreement No. ERC-ADG-2021-101052956-BEYOND).

Experiments were performed (i.) at MUSAM (IMT Lucca) using equipment purchased with the support of the grants: ERC StG CA2PVM (Grant Agreement 306622), ERC PoC PHYSIC (Grant Agreement No. 737447), (ii.) at the Instabilities Lab (University of Trento), and (iii.) at the Laboratory for Numerical Modelling of Materials (University of Trento), using equipment purchased with the support of the grants: ERC-ADG-2021-101052956-BEYOND and ERC-2013-ADG-340561-INSTABILITIES.

This work has been partially supported by the Italian Ministry of University and Research (MUR) through the project 'Scientific computing for natural sciences, social sciences, and applications: methodological and technological development' (PRO3 Joint Program 2022-23, CUP D67G22000130001), which is gratefully acknowledged by P.L. and M.P.

R.C. acknowledges financial support from project 'Studying the Colloidal Effect on the Spreading of Carbon-Based Agents on Hair' funded by 'Procter & Gamble Company'.

Appendix A. Supporting material

A.1. Biomorphic apatite

Two micrographs are reported in Extended Data Fig. 1, showing the cylindrical and non-overlapping nature of the porosity in the Biomorphic Apatite. The peculiar porosity results from the biomorphic transformation of rattan wood, used to produce the ceramic [13]. The voids do not overlap and run almost parallel to each other.

A.2. Code for the automatic generation of in-silico samples

The following code was implemented in the software Wolfram Mathematica 13.2 to generate samples through a random placing of circular voids in a rectangular specimen.

```
findPoints=
  Compile[{{n, _Integer},{lowX, _Real},{lowY, _Real}, {highX,_Real},{highY,
     _Real},{minD, _Real}},
   Block[{data = {{RandomReal[{lowX, highX}, 1][[1]],
        RandomReal[{lowY, highY}, 1][[1]]}}, k=1, rv, temp},
    While[k<n,
     rv = {RandomReal[{lowX, highX}, 1][[1]], RandomReal[{lowY,
      highY}, 1][[1]]};
     temp = Transpose[Transpose[data] - rv];
     If[Min[Sqrt[(#.#)]&/@ temp]>minD, data = Join[data, {rv}];
```

```
      k++;
      ];
     ];
    data]];

average =.; (* mean value of the normal distribution of voids' radii *)
stdev =.;  (* standard deviation of the normal distribution of voids' radii *)
npts = 10; (* number of voids to be randomly placed in a rectangular specimen *)
randomradius = RandomVariate[NormalDistribution[average,stdev],npts];
minD = 2.05 Quantile[randomradius, 0.999]; (* to avoid overlapping voids *)
lowX = 0;
highX = 4.5; (* Width of the specimen *)
lowY = 0;
highY = 9; (* Height of the specimen *)

pts = findPoints[npts,lowX,lowY,highX,highY,minD];

Graphics[{{EdgeForm[Black],White,Rectangle[{lowX,lowY}-1.5
    Quantile[randomradius, 1],{highX,highY}+1.5 Quantile[
    randomradius, 1]]}, Table[Circle[pts[[i]], randomradius[[i]]],
    {i,1,Dimensions[pts][[1]]}]}]
porosity = Sum[\[Pi]randomradius[[i]]^2,{i,1,Dimensions[pts[[1]]]}]/(
    highX highY) 100
```

A.3. An example of FEniCS code used for the phase-field simulations

The following code was written in Python language and implemented in FEniCS for the phase-field simulations of compression tests of rectangular samples characterized by 10% macro-porosity.

```
# Preliminaries and mesh
from dolfin import *
from mshr import *
from fenics import *
import sympy as sp
import numpy as np

N = 200 # mesh density

# Dimensions of the rectangular specimen.
L=4.5    # Dimension parallel to the loading direction
H=9

domain = Rectangle(Point(0.0,0.0), Point(L, H))\
-Circle(Point(3.0234,1.32474),0.200989)\
-Circle(Point(1.08572,0.914887),0.130479)\
-Circle(Point(1.90868,4.34213),0.121515)\
-Circle(Point(1.60387,5.6856),0.156055)\
-Circle(Point(1.19912,7.35778),0.131318)\
-Circle(Point(3.36847,3.88493),0.173114)\
-Circle(Point(2.90055,4.82629),0.178513)\
-Circle(Point(4.02467,2.21994),0.130005)\
-Circle(Point(0.962283,3.70378),0.12214)\
-Circle(Point(2.33,4.55591),0.131623)\
-Circle(Point(3.4486,5.76657),0.182436)\
-Circle(Point(1.91112,7.6117),0.164998)\
-Circle(Point(2.44688,0.72838),0.184461)\
-Circle(Point(1.70415,3.62776),0.180363)\
-Circle(Point(3.35107,6.89623),0.164833)\
-Circle(Point(3.27043,1.75659),0.181709)\
-Circle(Point(2.34352,1.35264),0.159497)\
-Circle(Point(3.03574,8.51386),0.152183)\
-Circle(Point(1.46163,2.22812),0.16439)\
-Circle(Point(1.5093,8.08228),0.163185)\
-Circle(Point(2.17844,6.26656),0.102296)\
-Circle(Point(1.99024,6.75547),0.133753)\
-Circle(Point(3.66352,8.35351),0.172959)\
-Circle(Point(1.03372,5.5871),0.159102)\
-Circle(Point(2.93496,2.88294),0.157626)\
-Circle(Point(3.87797,1.78228),0.15366)\
-Circle(Point(2.79145,8.09159),0.177494)\
-Circle(Point(3.35845,5.18456),0.18442)\
-Circle(Point(1.0558,4.18037),0.141059)\
-Circle(Point(3.74802,0.691879),0.133691)\
-Circle(Point(3.43903,7.45755),0.141225)\
-Circle(Point(0.455644,1.29338),0.217278)\
-Circle(Point(1.61206,0.47063),0.161412)\
-Circle(Point(0.811631,3.01581),0.172358)\
-Circle(Point(0.788551,2.30062),0.184847)\
-Circle(Point(1.12189,8.50223),0.123125)\
-Circle(Point(3.24528,0.89577),0.168204)\
-Circle(Point(3.35042,4.39078),0.160364)\
-Circle(Point(2.40094,3.94387),0.206106)\
-Circle(Point(2.20688,8.31152),0.154431)\
-Circle(Point(1.51481,4.82766),0.199603)\
-Circle(Point(2.88458,6.14344),0.171904)\
-Circle(Point(2.0923,5.0049),0.157516)\
-Circle(Point(1.80456,1.13777),0.158846)\
-Circle(Point(2.41821,3.50223),0.142688)\
-Circle(Point(2.91964,5.57736),0.147211)\
-Circle(Point(2.05032,5.51792),0.188997)\
-Circle(Point(2.48433,5.62876),0.174551)\
-Circle(Point(1.06665,1.52626),0.174677)\
-Circle(Point(2.43591,2.99175),0.146721)\
-Circle(Point(2.10898,1.85966),0.130821)\
-Circle(Point(0.637225,5.22015),0.156965)\
-Circle(Point(0.926142,6.79028),0.191514)\
-Circle(Point(0.958435,0.43857),0.140543)\
-Circle(Point(2.62284,7.55941),0.129576)

mesh = generate_mesh(domain, N)    # Generate mesh of the domain

# Define Space
V = FunctionSpace(mesh, 'CG', 1)
W = VectorFunctionSpace(mesh, 'CG', 1)
WW = FunctionSpace(mesh, 'DG', 0)
p, q = TrialFunction(V), TestFunction(V)
pnew, pold, Hold = Function(V), Function(V), Function(V)

# Introduce manually the parameters for a linear elastic
    perfectly brittle
# material under plane stress loading
E= 70                       # Young's Modulus
nuu =0.25                   # Poisson ratio
lmbda =  E*nuu/(1-nuu**2)   # First Lame' constant
mu =  E/(2*(1+nuu))         # Second Lame' constant
Gc=0.0025                   # Griffith critical surface energy
l= 0.012                    # Regularisation length

tol=1E-8
kappa=1e-6                  # Residual stiffness.

# Introducing strain energy density split

# Measures of strain
def epsilon(u):
    return sym(grad(u))

# Positive strain: strain associated with positive eigenvalues
# of the strain tensor
def strn_p(u):
    t = sym(grad(u))

    v00= (t[0, 0] + t[1, 1])/2 + sqrt(((t[0,0]-t[1,1])/2)**2+(t
     [1,0])**2)
    v01= 0
    v10= 0
    v11= (t[0, 0] + t[1, 1])/2 - sqrt(((t[0,0]-t[1,1])/2)**2+(t
     [1,0])**2)

    cons1 = 1/sqrt(1+((v00-t[0,0])/t[1,0])**2)
    cons2 = 1/sqrt(1+((v11-t[0,0])/t[1,0])**2)
    w00 = cons1
    w01 = cons2
    w10 = cons1*(v00-t[0,0])/t[1,0]
    w11 = cons2*(v11-t[0,0])/t[1,0]

    wp = ([w00,w01],[w10,w11])
    wp = as_tensor(wp)

    wp_tr = ([w00,w10],[w01,w11])
    wp_tr = as_tensor(wp_tr)

    v00 = conditional(gt(v00,0.0),v00,0.0)
    v11 = conditional(gt(v11,0.0),v11,0.0)

    vp = ([v00,v01],[v10,v11])
    vp = as_tensor(vp)
    return wp*vp*wp_tr
```

```
# Negative strain: strain associated with negative eigenvalues
# of the strain tensor
def strn_n(u):
    t = sym(grad(u))

    v00= (t[0, 0] + t[1, 1])/2 + sqrt(((t[0,0]-t[1,1])/2)**2+(t[1,0])**2)
    v01= 0
    v10= 0
    v11= (t[0, 0] + t[1, 1])/2 - sqrt(((t[0,0]-t[1,1])/2)**2+(t[1,0])**2)

    cons1 = 1/sqrt(1+((v00-t[0,0])/t[1,0])**2)
    cons2 = 1/sqrt(1+((v11-t[0,0])/t[1,0])**2)
    w00 = cons1
    w01 = cons2
    w10 = cons1*(v00-t[0,0])/t[1,0]
    w11 = cons2*(v11-t[0,0])/t[1,0]

    wn = ([w00,w01],[w10,w11])
    wn = as_tensor(wn)

    wn_tr = ([w00,w10],[w01,w11])
    wn_tr = as_tensor(wn_tr)

    v00 = conditional(lt(v00,0.0),v00,0.0)
    v11 = conditional(lt(v11,0.0),v11,0.0)

    vn = ([v00,v01],[v10,v11])
    vn = as_tensor(vn)
    return wn*vn*wn_tr

#Part of the energy associated with the positive strain
def psi(u):
    return 0.5*lmbda*(0.5*(tr(epsilon(u))+abs(tr(epsilon(u)))))**2
    +mu*tr(strn_p(u)*strn_p(u))

#Part of the energy associated with the negative strain
def psi_n(u):
    return 0.5*lmbda*(0.5*(tr(epsilon(u))-abs(tr(epsilon(u)))))**2
    +mu*tr(strn_n(u)*strn_n(u))

# Strain history function, accounting for the irreversibility of crack formation
def H(uold,unew,Hold):
    return conditional(lt(psi(uold),psi(unew)),psi(unew),Hold)

# Boundary conditions
right = CompiledSubDomain("near(x[0], 4.5) && on_boundary")
left  = CompiledSubDomain("near(x[0], 0.0) && on_boundary")
def left1(x, on_boundary):
    return abs(x[1]-4.5) < 1e-01 and on_boundary

load = Expression("t", t = 0.0, degree=1)
bcleft =  DirichletBC(W.sub(0), Constant(0.0), left )
bcleft1=  DirichletBC(W.sub(1), Constant(0.0), left1)
bcright=  DirichletBC(W.sub(0), load, right)
bc_u = [bcright, bcleft, bcleft1]
boundaries = MeshFunction("size_t", mesh, mesh.topology().dim() - 1)
boundaries.set_all(0)
left.mark(boundaries,1)
ds = Measure("ds")(subdomain_data=boundaries)
n = FacetNormal(mesh)

# Cauchy stress.
def sigma(u):
    return 2.0*mu*epsilon(u)+lmbda*tr(epsilon(u))*Identity(len(u))

# Cauchy stress associated with the positive strain energy
def sigma_p(u):
    return lmbda*0.5*(tr(epsilon(u))+abs(tr(epsilon(u))))*Identity(len(u))
    +2.0*mu*strn_p(u)

# Cauchy stress associated with the negative strain energy
def sigma_n(u):
    return lmbda*0.5*(tr(epsilon(u))-abs(tr(epsilon(u))))*Identity(len(u))
    +2.0*mu*strn_n(u)

x = SpatialCoordinate(mesh)

du = TrialFunction(W)
v = TestFunction(W)

# Variational form
unew, uold = Function(W), Function(W)

# set up solution functions
u = Function(W,name='displacement')

# The way the eigenvalues are computed one cannot allow
# a constant value of u at the start

u_array = u.vector().get_local()
u_array = np.random.rand(len(u_array))
u.vector()[:] = u_array

# Weak form of the mechanical problem
F_u = (((1.0-pold)**2+kappa)*inner(grad(v),sigma_p(u))+inner(grad(v),sigma_n(u)))*dx
J_u = derivative(F_u, u, du )
p_disp = NonlinearVariationalProblem(F_u, u, bc_u, J_u)
solver_disp  = NonlinearVariationalSolver(p_disp)

# Weak form of the evolutive problem
E_phi = (Gc*l*inner(grad(p),grad(q))+
((Gc/l)+2.0*H(uold,unew,Hold))*inner(p,q)-2.0*H(uold,unew,Hold)*q)*dx
p_phi  = LinearVariationalProblem(lhs(E_phi), rhs(E_phi),pnew)
solver_phi  = LinearVariationalSolver(p_phi)

# Initialization of the iterative procedure and output requests
t = 0
u_r1 = -1.0*1e-3            # Imposed displacement
u_r2 = -3.0*1e-5
deltaT  = 1.0

conc_f = File ("./PHASE/phi.pvd")
u_f    = File ("./DISPL/u.pvd")
fname  = open('ForcevsDisp.txt', 'w')
fname1 = open('Strain_energy.txt','w')
fname2 = open('Dissipated_energy.txt','w')

# Definition of the total elastic energy and total dissipated energy
def E_strain(u,pold):
    return (((1.0-pold)**2+kappa)*psi(u)+psi_n(u))*dx
def E_dissip(p):
    return ((Gc/2)*l*inner(grad(p),grad(p))+(Gc/(2*l))*p**2)*dx

T1 = 400
T2 = 0
Tmax=T1+T2


# Staggered scheme
while t<=Tmax:
    t += deltaT
    if(t<=T1):
       load.t+=u_r1
    if(t>T1):
       load.t+=u_r2

    solver_disp.solve()

    uold.assign(unew)
    unew.assign(u)

    solver_phi.solve()

    pold.assign(pnew)

    Hold.assign(project(psi(unew), WW))
```

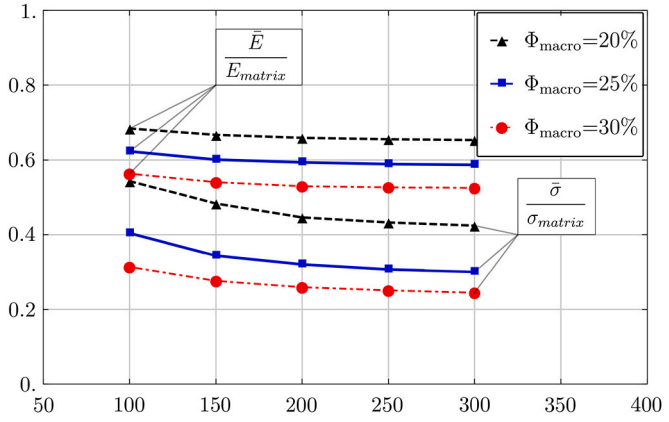

Extended Data Fig. 2. Sensitivity analysis of the phase field simulation on mesh refinement. Convergence of peak stress and overall Young's modulus for increasing number of nodes of the finite element mesh in the direction parallel to loading.

```
    print ('Iterations:', iter, ', Total time', t)
    if (t % 5) == 0: # stampa ogni 5 timestep
        conc_f << pnew
        u_f << unew
    Traction = dot(sigma(unew),n)
    fx = Traction[0]*ds(1)
    fname1.write(str(t) + "\t")
    fname1.write(str(assemble(E_strain(unew,pnew))) + "\n")
    fname2.write(str(t) + "\t")
    fname2.write(str(assemble(E_dissip(pnew))) + "\n")
    print ('traction:', iter, ', Total time', fx)
    #fname.write(str(t*u_r) + "\t")
    fname.write(str(assemble(fx)) + "\n")

fname.close()
print ('Simulation completed')
```

Sensitivity of the code to the mesh size was tested in order to calibrate the mesh size for subsequent numerical analyses. Extended Data Fig. 2 shows the results.

Here, compression tests for three values of single-scale porosity are simulated with generated in-silico specimens. Simulations are performed with 5 different meshes of increasing number of elements, to assess the sensitivity to the mesh refinement. Meshes, generated with isoparametric linear triangular finite elements, are characterized by the number h of nodes (examples are reported in Fig. 3), discretizing the side L of samples parallel to the loading, so that the values $h = \{100, 150, 200, 250, 300\}$ have been considered. In order to find the value of h for which the solution becomes mesh-independent, strength (in terms of overall peak stress $\bar{\sigma}$) and stiffness (in terms of overall Young's Modulus $\bar{E}$) have been evaluated. Results are presented in Fig. 2, where $\bar{E}$ and $\bar{\sigma}$ are made dimensionless respectively through division by the Young's modulus and by the value of the peak stress in tension, both referred to the matrix material. Fig. 2 shows that independence of mesh size is achieved for $h \geq 200$, so that $h = 200$ is selected for the subsequent evaluations.

A.4. Single-scale porosity

A schematic representation of the samples and the loading conditions used in the numerical simulations when a single scale of porosity is only present, is sketched in the inset of Extended Data Fig. 3. Results of numerical simulations of compression tests of porous brittle material using the phase-field approach to fracture are summarized in Extended Data Table 1, where the overall Young's modulus ($\overline{\mathrm{E}}$) and Peak stress ($\overline{\sigma}$) are reported for each specimen along with its porosity.

Overall stress-strain curves shown in Extended Data Fig. 3 have been obtained by averaging over ten simulations, for each level of macro-porosity (sketched on the top of the figure). The corresponding evolution of the phase-field, representing crack patterns, is shown in Extended Data Fig. 3, along with the deformed mesh. As clearly visible, cracks progressively develop parallel to the direction of the applied load. Extended Data Fig. 3 shows that the model can effectively capture damage nucleation, fracture propagation, and the final failure mechanism.

Well-formed crack patterns at a strain level close to collapse are reported in the upper part of Extended Data Fig. 3 for all samples

Extended Data Table 1

Overall properties of specimen with single scale voids. Summary of the overall properties of single scale brittle porous specimen with a single scale of porosity according to phase-field approach to fracture mechanics.

Φ_{macro}	$\overline{\mathrm{E}}$ [MPa]	$\overline{\sigma}$ [MPa]	Φ_{macro}	$\overline{\mathrm{E}}$ [MPa]	$\overline{\sigma}$ [MPa]
0%	70.00	7.27	25%	39.19	1.80
5%	61.87	4.42	25%	39.84	1.78
5%	61.69	4.61	25%	38.50	1.55
5%	62.05	4.37	25%	37.93	1.47
5%	61.78	4.49	25%	38.65	1.83
5%	61.83	4.76	25%	37.77	1.39
5%	61.86	4.60	25%	37.77	1.89
5%	62.20	4.52	25%	38.51	1.91
5%	61.79	4.84	25%	38.95	1.98
5%	62.16	4.31	30%	37.13	1.87
5%	62.02	4.39	30%	35.73	1.68
10%	54.88	3.40	30%	34.69	1.65
10%	55.56	3.47	30%	34.15	1.26
10%	55.55	3.16	30%	34.32	1.54
10%	55.04	3.30	30%	34.19	1.27
10%	55.30	3.66	30%	33.86	1.57
10%	55.34	3.29	30%	33.05	1.48
10%	55.34	3.11	30%	32.64	1.42
10%	55.03	3.51	30%	33.82	1.52
10%	55.14	3.30	32%	33.72	1.67
10%	55.18	3.16	32%	32.75	1.54
15%	51.09	3.26	32%	33.95	1.59
15%	48.97	2.62	35%	29.47	1.14
15%	49.26	2.63	35%	30.03	1.12
15%	49.27	2.67	35%	29.37	1.30
15%	48.92	2.69	35%	29.40	1.23
15%	48.84	2.77	35%	29.82	1.25
15%	48.29	2.79	35%	29.13	1.22
15%	48.64	2.45	35%	30.01	1.39
15%	49.02	3.00	35%	30.29	1.24
15%	48.34	2.79	35%	30.35	1.34
20%	46.15	2.43	35%	30.40	1.24
20%	43.67	2.21	40%	22.21	0.79
20%	44.30	2.18	40%	23.33	0.97
20%	42.82	1.88	40%	23.37	0.94
20%	43.16	2.12	40%	25.49	0.98
20%	43.08	2.16	40%	26.01	1.15
20%	42.95	1.93	40%	26.45	1.06
20%	42.44	1.87	40%	26.24	1.17
20%	43.77	2.20	40%	26.25	1.16
20%	43.07	2.26	40%	25.88	1.04
25%	41.57	2.01	40%	26.34	1.12

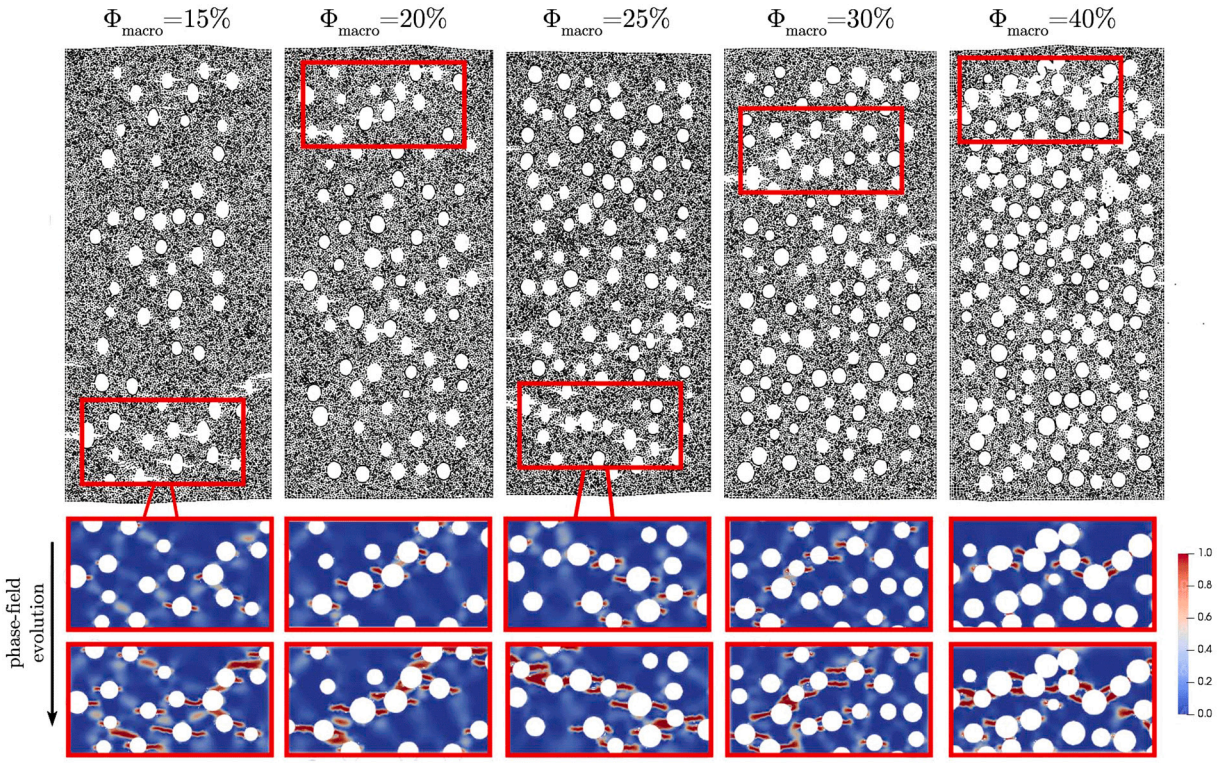

Extended Data Fig. 3. Phase field simulation of crack propagation in biomorphic apatite, where only one scale of porosity is considered. Deformed meshes (upper part) at an overall strain close to the strain at the collapse and phase-field evolution (lower part) at two levels of overall strain $\bar{\varepsilon}$ ranging between 5×10^{-2} and 7×10^{-2}, for samples of different porosity, tested under uniaxial compression in the horizontal direction.

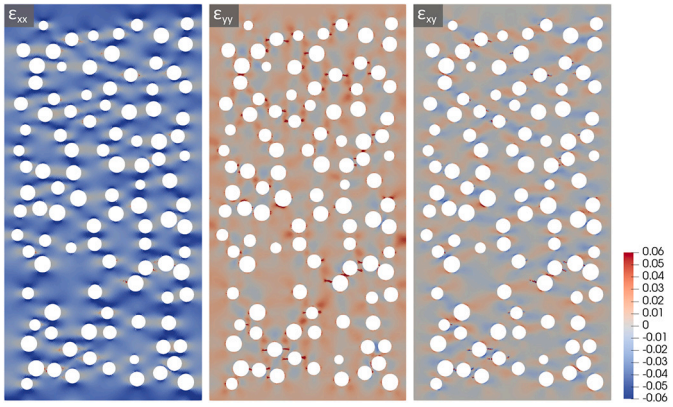

Extended Data Fig. 4. Components of the strain tensor in a specimen with 25% macro-porosity for an imposed lateral displacement of 0.2 mm, corresponding to an estimated average axial strain of $\overline{\varepsilon} \approx 0.04$.

shown in Extended Data Fig. 3. In the lower part of the same figure, the phase-field shows that cracks grow parallel to the loading direction, independently of the porosity. To highlight fracture growth, the lower part of the figure reports details of the samples at two levels of overall strain $\bar{\varepsilon}$ ranging between 5×10^{-2} and 7×10^{-2}.

A.5. Strain within the samples

Simulations of compression tests on porous material are carried out until overall strains equal to 0.1. These values are moderately large and can be decomposed into a relatively small strain in the matrix material and large rigid-body displacements of blocks separated by intense zones of damage. In fact, the maps of the three strain components reported in Extended Data Fig. 4 show that intense strains only occur in narrow zones of highly deformed material.

A.6. Two-scale porosity

In Extended Data Table 2 a summary of the results is reported (in terms of overall Young's Modulus and peak stress) of the simulations carried out for the samples characterized by two scales of porosity.

Appendix B. Supplementary material

Supplementary material related to this article can be found online at https://doi.org/10.1016/j.matdes.2024.112708.

Extended Data Table 2
Overall response of specimen with voids of different size. Summary of the results – in terms of overall Young's Modulus and peak stress – of the simulations carried out for the samples with two scales of porosity.

Φ_{macro}	Φ_{meso}	Φ	$\overline{E}$ [MPa]	$\overline{\sigma}$ [MPa]
0%	0%	0%	70.00	7.27
10%	0%	10%	54.35	3.34
15%	0%	15%	48.66	2.52
10%	5%	15%	50.49	3.00
15%	2%	17%	46.85	2.40
15%	3%	18%	46.12	2.35
15%	5%	20%	44.87	2.34
20%	0%	20%	46.15	2.43
10%	10%	20%	46.87	2.72
15%	10%	25%	41.43	2.26
25%	0%	25%	37.26	1.67
20%	5%	25%	40.56	2.07
25%	2%	27%	35.62	1.52
25%	3%	28%	35.09	1.53
25%	5%	30%	34.04	1.51
30%	0%	30%	33.31	1.40
20%	10%	30%	37.65	2.00
25%	7%	32%	32.45	1.45
30%	2%	32%	31.76	1.31
32%	0%	32%	30.83	1.22
30%	3%	33%	31.39	1.31
32%	2%	34%	29.32	1.10
25%	10%	35%	31.62	1.44
30%	5%	35%	30.30	1.26
32%	3%	35%	28.87	1.08
35%	0%	35%	29.67	1.28
32%	5%	37%	28.08	1.05
35%	5%	40%	26.86	1.17
30%	10%	40%	28.17	1.24
40%	0%	40%	25.50	0.95
32%	10%	42%	25.92	1.01
40%	2%	42%	24.06	0.88
40%	3%	43%	23.70	0.87
35%	10%	45%	26.01	1.13
40%	5%	45%	23.01	0.86
40%	10%	50%	21.42	0.85

References

[1] S. Sprio, S. Pansieri, M. Montesi, et al., Hierarchical porosity inherited by natural sources affects the mechanical behaviour and biological behaviour of bone scaffolds, J. Eur. Ceram. Soc. 40 (2020) 1717–1727.
[2] H. Wang, Y. Tang, P. Bai, W. Guo, Y. Luo, S. Li, X. Zhang, G. Zhou, A multiscale composite silicon carbide wick with excellent capillary performance, Int. Commun. Heat Mass Transf. 139 (2022).
[3] E. Wölfel, I. Fiedler, S.D. Kolibova, J. Krug, M. Lin, B. Yazigi, A. Siebels, H. Mushumba, B. Wulff, B. Ondruschka, K. Püschel, C. Glüer, K. Jähn-Rickert, B. Busse, Human tibial cortical bone with high porosity in type 2 diabetes mellitus is accompanied by distinctive bone material properties, Bone 165 (2022) 116546.
[4] A. Sombatmai, V. Uthaisangsuk, S. Wongwises, P. Promoppatum, Multiscale investigation of the influence of geometrical imperfections, porosity, and size-dependent features on mechanical behavior of additively manufactured Ti-6Al-4V lattice struts, Mater. Des. 209 (2021) 109985.
[5] J. Heath, T. Dewers, H. Yoon, P. Mozley, Multiscale porosity and mechanical properties of mancos shale: evaluation of rev and scale separation, in: American Geophysical Union, Fall Meeting, 2016, p. 2016.
[6] A. Özen, G. Ganzosch, C. Völlmecke, D. Auhl, Characterization and multiscale modeling of the mechanical properties for fdm-printed copper-reinforced PLA composites, Polymers (Basel) 14 (2022) 3512.
[7] D. Gupta, P. Vashisth, J. Bellare, Multiscale porosity in a 3d printed gellan-gelatin composite for bone tissue engineering, Biomed. Mater. 16 (2021).
[8] A. Baux, L. Nouvian, K. Arnaud, S. Jacques, T. Piquero, D. Rochais, P. David, G. Chollon, Synthesis and properties of multiscale porosity tic-sic ceramics, J. Eur. Ceram. Soc. 38 (2019) 2601–2616.
[9] F. Senhora, E. Sanders, G. Paulino, Optimally-tailored spinodal architected materials for multiscale design and manufacturing, Adv. Mater. 34 (2022) 2109304.
[10] M. Gomez-Cerezo, J. Peña, S. Ivanovski, D. Arcos, M. Vallet-Regi', C. Vaquette, Multiscale porosity in mesoporous bioglass 3d-printed scaffolds for bone regeneration, Mater. Sci. Eng. C, Mater. Biol. Appl. 120 (2021).
[11] J. Clayton, J. Zorn, R. Leavy, M. Guziewski, J. Knap, Phase field modeling of diamond-silicon carbide ceramic composites with tertiary grain boundary phases, Int. J. Fract. 237 (2022) 101–138.
[12] A. Tampieri, A. Ruffini, A. Ballardini, M. Montesi, S. Panseri, F. Salamanna, M. Fini, S. Sprio, Heterogeneous chemistry in the 3-d state: an original approach to generate bioactive, Biomater. Sci. 7 (2019) 307–321.
[13] D. Bigoni, R. Cavuoto, D. Misseroni, M. Paggi, A. Ruffini, S. Sprio, A. Tampieri, Ceramics with the signature of wood: a mechanical insight, Materials Today Bio 5 (2019) 100032.
[14] A.P. Roberts, E.J. Garboczi, Elastic properties of model porous ceramics, J. Am. Ceram. Soc. 83 (2000) 3041–3048.
[15] W. Pabst, E. Gregorova, G. Ticha, Elasticity of porous ceramics - a critical study of modulus-porosity relations, J. Eur. Ceram. Soc. 26 (2006) 1085–1097.
[16] C.G. Sammis, M.F. Ashby, The failure of brittle porous solids under compressive stress states, Acta Metall. 34 (1986) 511–526.
[17] M. Kachanov, Elastic solids with many cracks and related problems, Adv. Appl. Mech. 30 (1993) 259–445.
[18] A. Gustafsson, M. Wallin, H. Isaksson, The influence of microstructure on crack propagation in cortical bone at the mesoscale, J. Biomech. 112 (2020) 110020.
[19] S. Karthik, K. Reddy, A. Nasedkina, A. Nasedkin, A. Rajagopal, Phase field vs gradient enhanced damage models: a comparative study, Proc. Struct. Integrity 35 (2022) 173–180.
[20] Z. Bažant, Why continuum damage is nonlocal: micromechanics arguments, J. Eng. Mech. 117 (1990) 1070–1087.
[21] Z. Bažant, M. Jirasek, Damage nonlocality due to microcrack interactions: statistical determination of crack influence function, in: Fracture and Damage in Quasibrittle Structures E & F Spon Pubs, 1994, pp. 3–17.
[22] T. Bui, H. Tran, Numerical simulations of dynamic fracture and fragmentation problems by a novel diffusive damage model, Comput. Math. Appl. 125 (2022) 193–212.
[23] G. Francfort, J. Marigo, Revisiting brittle fracture as an energy minimization problem, J. Mech. Phys. Solids 46 (1998) 1319–1342.
[24] B. Bourdin, G. Francfort, J. Marigo, The variational approach to fracture, J. Elast. 91 (2008) 5–148.
[25] G.D. Maso, R. Toader, A model for the quasistatic growth of brittle fractures: existence and approximation results, Arch. Ration. Mech. Anal. 162 (2002) 101–135.
[26] L. Ambrosio, V. Tortorelli, Approximation of functionals depending on jumps by elliptic functionals via Γ-convergence, Commun. Pure Appl. Math. 43 (1990) 999–1036.
[27] G.D. Maso, An Introduction to Γ-Convergence, Progress in Nonlinear Differential Equations and Their Application, 1993.
[28] D. Braides, Approximation of Free Discontinuity Problems, Springer Verlag, Berlin, 1998.
[29] C. Miehe, M. Hofacker, F. Welschinger, A phase field model for rate-independent crack propagation: robust algorithmic implementation based on operator splits, Comput. Methods Appl. Mech. Eng. 199 (2010) 2765–2778.
[30] M. Geer, R. de Borst, W. Brekelmans, R. Peerlings, Strain-based transient gradient damage model for failure analysis, Comput. Methods Appl. Mech. Eng. 160 (1998) 133–154.
[31] R. Cavuoto, P. Lenarda, D. Misseroni, M. Paggi, D. Bigoni, Failure through crack propagation in components with holes and notches: an experimental assessment of the phase field model, Int. J. Solids Struct. 257 (2022) 111798.
[32] M. Borden, C. Verhoosel, M. Scott, T. Hughes, C. Landis, A phase-field description of dynamic brittle fracture, Comput. Methods Appl. Mech. Eng. 217–220 (2012) 77–95.
[33] W. Pabst, E. Gregorová, Note on the so-called Coble-Kingery formula for the effective tensile modulus of porous ceramics, J. Mater. Sci. Lett. 22 (2003) 952–962.
[34] W. Pabst, E. Gregorová, Derivation of the simplest exponential and power-law relations for the effective tensile modulus of porous ceramics via functional equations, J. Mater. Sci. Lett. 22 (2003) 1673–1675.
[35] W. Pabst, E. Gregorová, Effective elastic properties of alumina-zirconia composite ceramics - Part 2. Micromechanical modeling, Ceram.-Silik. 48 (2004) 14–23.
[36] R. Christensen, Effective properties of composite containing voids, Proc. R. Soc. Lond. A 440 (1993) 461–473.
[37] R. Rice, Porosity of Ceramics, Marcel Dekker Inc., 1998.
[38] Y. Cui, Y.F. Gao, H.B. Chew, Two-scale porosity effects on cohesive crack growth in a ductile media, Int. J. Solids Struct. 200–201 (2020) 188–197.